# Invasion of Gas into Mica Nanopores: A Molecular Dynamics Study

Chao Fang, Fei Zhang, and Rui Qiao\*

Department of Mechanical Engineering, Virginia Tech, Blacksburg, VA 24061, USA

ABSCTRACT: Invasion of gas into liquid-filled nanopores is encountered in many engineering problems but is not yet well understood. We report molecular dynamics simulations of the invasion of methane gas into water-filled mica pores with widths of 2-6nm. Gas invades into a pore only when the pressure exceeds a breakthrough pressure and a thin residual water film is left on the mica wall as the gas phase moves deeper into the pore. The gas breakthrough pressure of pores as narrow as 2nm can be modeled reasonably well by the capillary pressure if the finite thickness of residual liquid water film and the liquid-gas interface are taken into account. The movement of the front of the liquid meniscus during gas invasion can be quantitatively described using the classical hydrodynamics when the negative slip length on the strongly hydrophilic mica walls is taken into account. Understanding the molecular mechanisms underlying the gas invasion in the system studied here will form the foundation for quantitative prediction of gas invasion in practical porous media.

<sup>\*</sup> To whom correspondence should be addressed. Email: ruiqiao@vt.edu.

### 1. Introduction

The transport of multiphase fluids in nanopores plays a critical role in diverse areas including lab-on-chip, oil and gas recovery, smart textiles, and energy storage. <sup>1-4</sup> Driven by the technical needs in these areas and the advancements in nanochannel fabrication and computational methods, <sup>5</sup> there has been a surge of research activities in understanding these phenomena. In particular, much attention has focused on the imbibition and infiltration of fluids (both spontaneous and forced) into nanopores. These researches have revealed rich imbibition dynamic ranging from recovering the classical Washburn law in some systems to qualitative and quantitative deviations from the classical law in other systems. <sup>6-12</sup> For parameters such as the critical pressure for the infiltration of water into hydrophobic pores, it has been shown that the classical Young-Laplace equation cannot accurately predict the threshold pressure for carbon nanotubes. <sup>13-15</sup>

While the imbibition and infiltration of fluids into gas-filled pores have received much attention, the opposite process, i.e., the invasion of gas into liquid-filled pores, has received much less attention. Such a process is encountered in practical applications. For example, in shale gas recovery, the highly pressurized gas such as methane must sometime pass through water-saturated tight rocks featuring extensive nanopores before it can be recovered. Of the few existing studies, most are experimental characterization of the gas invasion process into water-saturated rock samples. While these studies provided valuable data on the gas invasion process in practical systems, the complexity of the systems studied (e.g., heterogeneity of surface properties and size of the pores in the rock samples) makes it challenging to gain generalized insight into the gas invasion process. To address this challenge, studies of the gas invasion process at the pore scale can be very useful.

Two important aspects of the invasion of gas into a liquid-filled pore are the gas breakthrough pressure  $P_B$  (i.e., the pressure above which gas can invade into the pore) and the dynamics of gas invasion at pressure higher than  $P_B$ . The breakthrough pressure is often taken as the capillary

pressure given by the Young-Laplace equation, i.e.,  $P_B = 2\gamma \cos\theta / R$  for a cylindrical pore and  $P_B = 2\gamma \cos\theta / W$  for a slit pore, where  $\gamma$  is the interfacial tension of the gas-liquid interface,  $\theta$  is the contact angle. R (W) is the radius (width) of cylindrical (slit) pore. The dynamics of the gas invasion into the pore is typically described using the Navier-Stokes equation with bulk liquid and gas properties. While these approaches should be accurate for wide pores, their accuracy in narrow nanopores is not immediately clear. For example, recent studies showed that the surface tension of liquids confined in nanopores can deviate from that of bulk liquids,  $^{20}$  and the viscosity of fluids confined in nanopores is non-uniform across the pore and can be much higher than that of bulk liquids. Given these interesting phenomena, it is useful to examine the invasion of gas into nanopores without making the assumptions in the classical approaches widely used in the literature.

In this work, we use molecular dynamics (MD) simulations to investigate the invasion of gas into mica nanopores with widths of 2, 4, and 6nm. We determine the gas breakthrough pressure and the dynamics of gas invasion and compare our observations with classical theories. The rest of this manuscript is organized as follows. In *Section 2*, the molecular model and simulation details are presented. In *Section 3*, the thermodynamics and dynamics of the gas invasion including the gas breakthrough pressure and invasion dynamics are discussed. Finally, conclusions are drawn in *Section 4*.

### 2. Simulation details

Figure 1 shows a schematic of the MD system for studying the breakthrough of methane gas into a slit-shaped nanopore initially filled with water. The system consists a slit pore cleaved from a mica slab and two reservoirs at the pore's two ends. Initially, the left reservoir features both a gas phase (methane, 8nm thick in the *x*-direction) and a liquid phase (water, 2nm thick in the *x*-direction). The large volume of methane molecules in the left reservoir ensures that the gas molecule can fill the entire slit pore after gas breakthrough occurs. The right reservoir only contains

water (3nm thick in the x-direction) initially. The desired pressure in the reservoirs is regulated by applying the necessary forces to the two rigid pistons bounding the reservoirs. The dimensions of the pore in the x- and y-directions are 14.7nm and 3.15nm, respectively. The pore width, defined as the distance between the surface potassium ions on the upper and lower mica walls (see Fig. 1), is W = 2, 4, and 6nm in different simulations. The MD system is periodic in all three directions. To effectively model systems that are periodic only in the y- and z-directions, two large vacuum spaces are placed outside the rigid pistons.

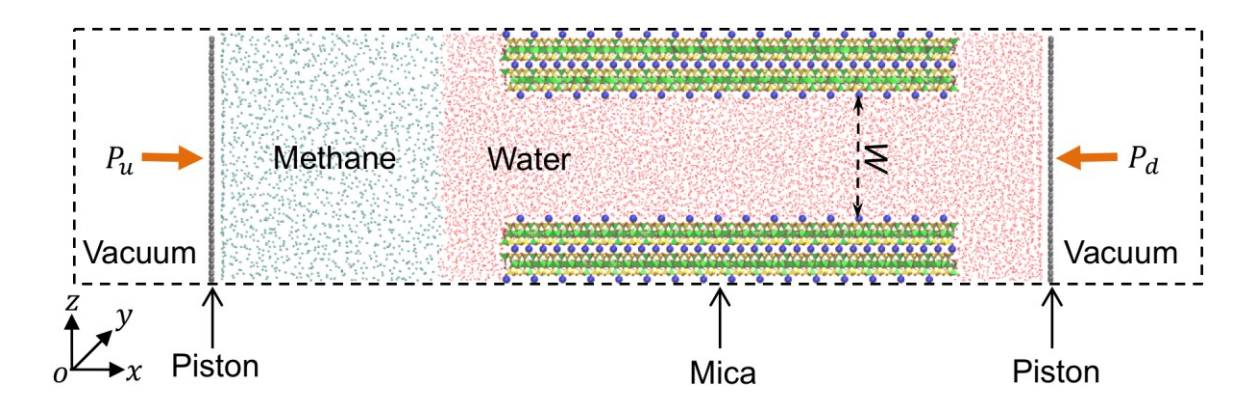


**Figure 1**. A snapshot of the molecular dynamics system for studying gas invasion into mica pores. The left reservoir is initially filled with 8nm thick (along x-direction) methane gas and 2nm thick (along x-direction) water. Water also fills the pore and a 3nm thick region (x-direction) in the right reservoir. Two rigid pistons are used to regulate the pressure in the two reservoirs. The pore is cleaved from bulk mica with a wall thickness of  $\sim$ 2nm. The pore width W (W= 2, 4, and 6nm) is the distance between the surface potassium ions (shown as blue spheres) of the two mica walls. The pore length is 14.7nm. The system is periodic in all three directions and the length in the y-direction is 3.1nm. Two large vacuum spaces are placed in the x-direction so that the system measures 40nm (W= 2, 4nm) or 45nm (W= 6nm) in the x-direction.

Each of the walls is made of two muscovite mica layers (~2nm thick) so that the liquid-wall interactions are captured accurately. Muscovite (KAl<sub>2</sub>Si<sub>3</sub>AlO<sub>10</sub>(OH)<sub>2</sub>) is a phyllosilicate clay and can be easily cleaved from the (001) plane.<sup>22</sup> Each muscovite layer has a tetrahedral-octahedral-tetrahedral (TOT) structure, in which each Al-centered octahedral sheet is sandwiched between two Si-centered tetrahedral sheets. Substitution of every four Si atoms in the tetrahedral layer by Al atoms results in a negative net charge, which is compensated by the K<sup>+</sup> ions. The neighboring TOT structures are then held together by a potassium interlayer. Following the widely used method

for building surfaces and nanopores from muscovite minerals, we cleave the muscovite from the (001) plane, resulting in a surface featuring  $K^+$  ions.<sup>22-23</sup> For simplicity, the surface  $K^+$  ions are arranged in ordered fashion following the previous approach.<sup>24-25</sup>

Water and methane are modeled using the SPC/E model and the TraPPE force fields,<sup>26</sup> respectively. The partial charges and LJ parameters of the mica atoms are taken from the CLAYFF force fields.<sup>22,27</sup> The TraPPE force fields enable accurate prediction of methane's thermodynamic properties. Prior works showed that the CLAYFF force fields allow the interfacial water on clay surfaces to be accurately modeled.<sup>23,28</sup> The interactions among mica atoms are excluded. All atoms in the clay sheets are tethered with a stiff spring. The piston atoms are modeled as Lennard-Jones atoms with parameters taken from those of the sp<sup>2</sup> carbon atoms in the OPLS-AA force fields. All force fields parameters are summarized in the Supplemental Material.

Simulations are carried out using the Gromacs package<sup>29</sup> in the NVT ensemble with a temperature T=400K. The temperature adopted here is relevant to that encountered in shale gas fields.<sup>30</sup> The temperature of the system is maintained using the velocity-rescaling thermostat.<sup>31</sup> The equations of motion are solved using a time step of 2fs during equilibrium runs and 1fs during non-equilibrium runs. Bond lengths and angles of the water molecules are fixed using the SETTLE algorithm. A cutoff 1.2nm is used for computing the Lennard-Jones potential and the particle mesh Ewald method is used for computing the electrostatic interactions.<sup>32</sup>

The MD system is first equilibrated for 4ns with  $P_u = P_d = P$  on both pistons (see Fig. 1). For the 2nm-wide pores, P is set to 100MPa; for the 4nm- and 6nm-wide pores, P is set to 60MPa. To initiate the invasion of methane gas into the nanopores, the pressure on the right piston ( $P_d$ ) is reduced while  $P_u$  is not changed. Note that, although using a lower pressure on the left piston ( $P_u$ ) is desirable, a high value is adopted because a lower pressure will require an extremely large volume of gas to be used in the simulations. Given that water has very low compressibility, adopting a relatively high  $P_u$  does not notably affect the gas invasion.

### 3. Results and discussions

### 3.1 Gas breakthrough characteristics

Figure 2a shows the snapshots of methane gas breaking into pores with widths of 2, 4, and 6 nm when the pressure difference between the up and down-stream reservoir ( $\Delta P_{ud}$ ) is sufficiently high. As the gas invades into the pores, a gas-water meniscus forms and moves toward the downstream reservoir. Importantly, as the meniscus moves downstream, a thin film of water is left on the mica surface. Such a liquid film forms due to the affinity of water to the strongly hydrophilic mica surface. Such a liquid film forms due to the affinity of water to the strongly hydrophilic mica surface. The formation of this residual film is akin to the formation of precursor films ahead of the moving meniscus when water is imbibed into pores (or when water droplets spread on substrates) with strongly hydrophilic walls. Algorithm for pores narrower than a few nanometers, such thin residual films occupy a substantial portion of the pore space. Moreover, as we shall see in Section 3.2, these thin residual films affect the critical gas breakthrough pressure in these narrow pores. Given the importance of these residual films, we characterize them in detail below.

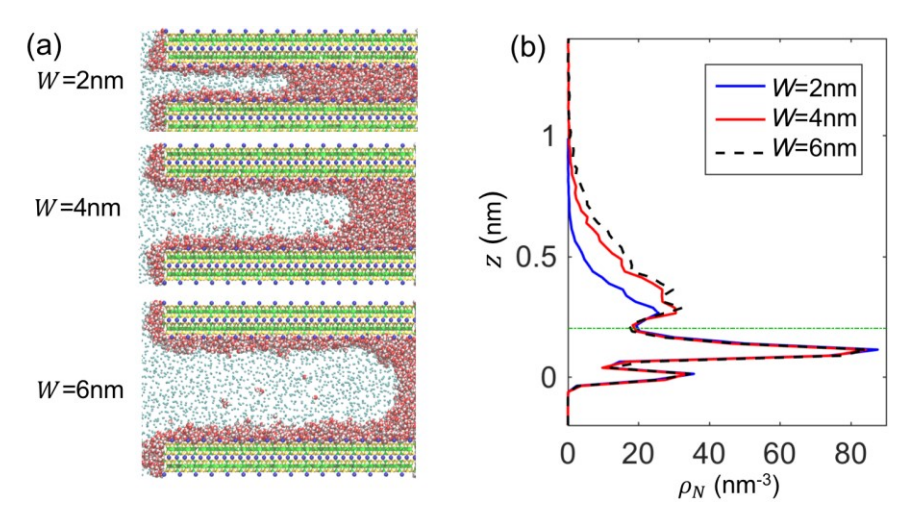


**Figure 2**. *Invasion of gas into water-filled mica pores*. (a) The snapshots of gas invasion into the 2, 4, and 6nm-wide pores. Methane molecules are shown as light blue spheres and water molecules are shown as red (oxygen) and white (hydrogen) spheres. The mica wall is the same as that in Fig. 1. (b) The number density profiles of water across the residual water films on the walls of the 2, 4, 6nm-wide pores (in the 2nm-wide pore,  $P_u$ =100MPa and  $P_d$ =10MPa; in the 4nm-wide pore,  $P_u$ =60MPa and  $P_d$ =20MPa; in the 6nm-wide pore,  $P_u$ =60MPa and  $P_d$ =40MPa.) The dashed line marks the water density valley at z=0.2nm, below which the water number density profiles are identical for the three pores.

We first compute the density distribution of the water residual film in direction normal to the mica wall. We focus on the portion of the water film 1.0nm away from the pore entrance and one pore width behind the moving meniscus, in which it has a nearly uniform thickness. In each pore, the density distribution is found to vary little once  $\Delta P_{ud}$  exceeds a critical breakthrough pressure  $P_B$  when the gas just begins to be able to break into the pore. Figure 2b shows the water density distribution across the thin residual films (note that the surface  $K^+$  ions are located at z=0) inside the 2, 4, and 6 nm pores. The density profiles show that water molecules can reach up to 1.0nm above the mica surface. For z < 0.2nm, the density profiles are practically identical in all pores; at z > 0.2nm, the water density becomes larger as the pore becomes wider, i.e., the residual water film thickens in wider pores. To quantify such a thickening, we follow the concept of the Gibbs dividing surface, and determine the residual film thickness by equating the surface excess from both the liquid and vapor sides along the wall normal direction z<sup>36</sup>

$$\int_{-\infty}^{h} [\rho_l - \rho(z)] dz = \int_{h}^{W/2} [\rho(z) - \rho_v] dz \tag{1}$$

where  $\rho_l$  and  $\rho_v$  are the densities of the saturated bulk liquid water and water vapor at 400K, respectively.  $\rho_l$  is taken to be 31.3nm<sup>-3</sup> based on independent simulations and  $\rho_v$  is taken as zero because it is much smaller than  $\rho_l$ . Using the density profiles shown in Fig. 2b, the thicknesses of the residual water films are determined as h=0.35, 0.49, and 0.54nm for 2, 4, and 6nm pores, respectively.

To clarify the thickening of the residual film in wider pores, we delineate the evolution of the residual water film when the pore size increases by examining the organization of water molecules in the film. By inspecting the snapshots of the water molecules in the residual water film (e.g., see Fig. 3a), one can identify two layers of water molecules in the residual film based on how the water molecules in the residual film interact with other molecules. The inner layer (z<0.2nm) consists of the water molecules hydrating the surface K<sup>+</sup> ions (cf. the density peak at  $z \sim 0.1$ nm) and the water molecules in the interstitial space between the surface K<sup>+</sup> ions (cf. the density peak at  $z \sim 0.02$ nm).

The outer layer consists of the water molecules that interact with the inner water layer.<sup>23, 25</sup> These two layers of water molecules can also be visualized by computing their distribution as a function of their radial and vertical distance from the surface  $K^+$  ions (see Fig. 3b; the surface  $K^+$  ions are located at (r, z) = (0, 0) and denoted by magenta dots).

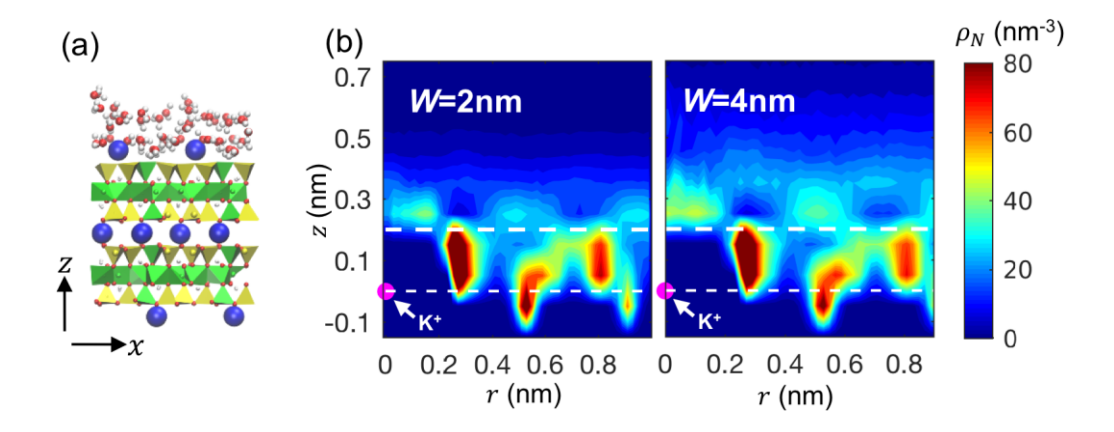


**Figure 3.** Molecular structure of the residual water film on mica walls. (a) A zoom-in view of the residual water layer near the mica wall of a 4nm-wide pore. The color coding is the same as Fig. 1 and Fig. 2a. (b) The number density distribution of water around mica's surface potassium ions in a cylindrical coordinate (r and z represent the radial and vertical distance of water molecules to the potassium ions, respectively). The number density distribution is calculated for the residual water film in W=2nm pore and W=4nm pore. The center potassium ions are shown in magenta dots. The position of the surface potassium ions (z=0) and the boundary for the inner/outer layer (z=0.2nm) is marked as dashed white lines.

Figure 2b and Fig. 3b show that, as the pore width increases from 2 to 4nm, the inner water layer hardly changes but the outer water layer becomes more distinct, i.e., the residual film grows by adding more water molecules to its outer layer without densifying or loosening its inner layer. This growth mode helps explain why the residual film becomes thicker as the pore width increases from 2 to 4nm. When gas breaks into a nanopore, the residual liquid films behind the meniscus are in quasi-equilibrium with the downstream water reservoir. Because the gas phase in contact with the residual film is at higher pressure than in the downstream reservoir, it tends to elevate the chemical potential of the water molecules inside the residual film above that in the downstream reservoir, and thus thins the residual film. However, the strong interactions between the water molecules in the residual film with the mica surface make these water molecules energetically

more favorable to stay in the residual film. The competition of these two processes results in a stable residual film with finite thickness. In narrow pores (e.g., W=2nm), the gas breakthrough pressure is high and thus the pressure of the gas phase in contact with the residual water film is high. Therefore, only water molecules interacting very strongly with the mica surface (i.e., mostly the inner water layer in Fig. 3b) can be stabilized. In wider pores (e.g., W=4 and 6nm), the pressure of the gas phase in contact with the water film is lower and thus even water molecules in the outer layer, which interact primarily with the inner water layer, can be stabilized. Therefore, the thickness of the residual water film increases as the pore becomes wider. We note that the thickening of the residual water film in larger pores is not influenced by the different  $P_u$  used in these simulations. Separate simulations show that, when the  $P_u$  increases to 100MPa in the 4nm-wide pores ( $P_d$  is increased accordingly), the film thickness is almost unchanged (see Fig. S1 in the Supplemental Material). Together, the thicker residual water films in larger pores should originate largely from the lower breakthrough pressures.

Thus far, we examined the basic process of gas invading mica pores and the formation of residual water film on pore walls. Below we examine two aspects of the gas invasion quantitatively: the gas breakthrough pressure and the dynamics of gas invasion into the mica pores.

#### 3.2 Gas breakthrough pressure

For each mica pore, a series of simulations with different  $\Delta P_{ud}$  are performed to check whether gas breakthrough occurs. A gas breakthrough occurs if continuous gas flow into the pore is observed. Once gas invades into a pore for more than the pore width W, the simulation is terminated. For cases in which gas breakthrough was not observed, the MD simulations are run for at least 20ns. The simulation results are summarized in Fig. 4, in which  $\Delta P_{ud}$  corresponding to observation of gas breakthrough is marked using blue stars and those corresponding to no gas invasion into the pore is marked using red squares.

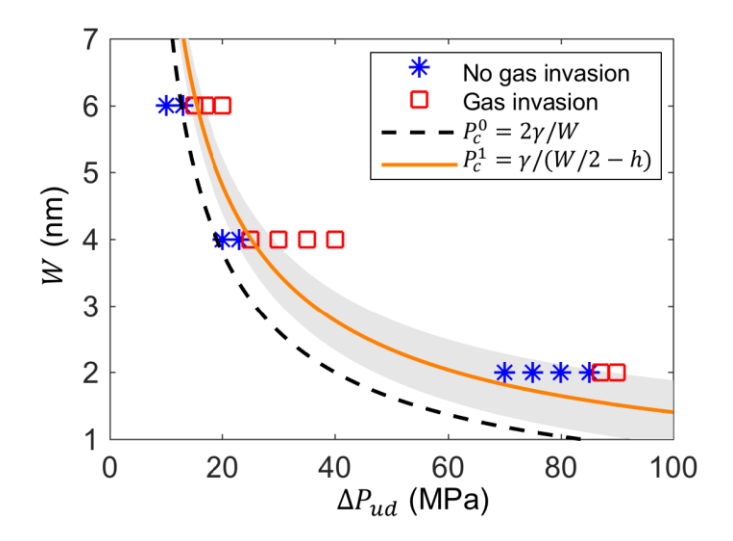


**Figure 4.** Gas breakthrough pressure in different pores. The pressure difference at which gas can (cannot) invade into the pore is shown as blue stars (red squares). The prediction of the gas breakthrough pressure by the classical capillary theory  $P_c^0 = 2\gamma/W$  is shown as a dashed line. The prediction by considering the narrowing of pores by the residual water film  $P_c^1 = \gamma/(W/2 - h)$  is shown as a solid line. The shaded area denotes the range of possible gas breakthrough pressure due to the ambiguity of assigning a thickness to the thin water films on the pore walls, which is in turn caused by the diffuseness of gas-liquid interfaces.

To check if gas breakthrough can be predicted using the capillary pressure (i.e.,  $P_B = P_c^0 = 2\gamma \cos\theta / w$ ), we note that separate simulation indicated that water droplets spread completely on the mica wall, i.e.,  $\theta=0$ . Since the methane-water interfacial tension depends on temperature and pressure, independent equilibrium simulations are performed to determine  $\gamma$ . In these simulations, a 4nm-thick slab of water is sandwiched between two 2nm slabs of methane (see Fig. 5). The number of methane molecules in the system is adjusted to give a methane pressure of 60, 80, and 100MPa, which is in the range of gas pressure in the gas breakthrough simulations. Each system is periodic in all three directions and the simulations are run in the NVT ensembles at three different temperatures. The methane-water interfacial tension is evaluated using  $\gamma = 1/2 \int_0^{L_X} [P_{xx} - 0.5(P_{yy} + P_{zz})] dx$ , <sup>37</sup> where  $L_x$  is the length of the simulation box in the direction normal to the water-methane interface (x-direction),  $P_{xx}$ ,  $P_{yy}$ , and  $P_{zz}$  are the three diagonal components of the pressure tensor along the x, y, and z-directions, respectively. To verify our calculations, we also compute the water-vacuum interfacial tension in a similar system at 300K, and obtain a value of  $61.4\pm0.9$ mN/m. This value agrees well with that in the literature for the same water model

(60.7mN/m), and it is lower than the experimental value (72.8 mN/m) mainly due to the choice of the water model.<sup>37</sup>

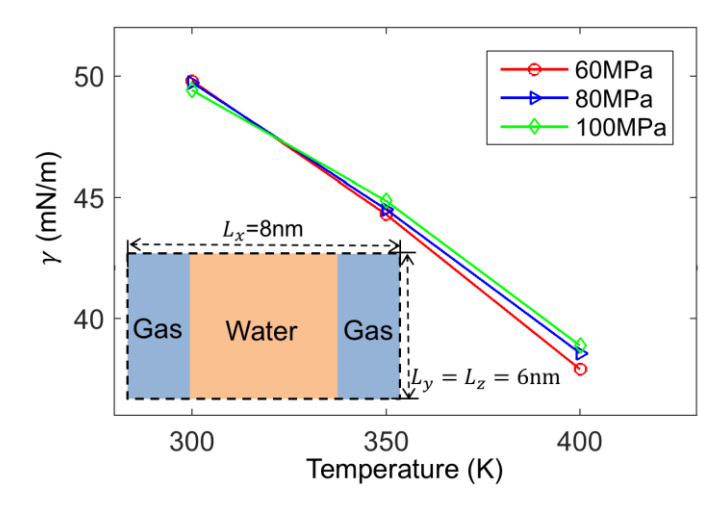


**Figure 5.** Water-methane interfacial surface tension. The inset is a schematic of the system used to compute the interfacial tension of planar water-methane interfaces.

Figure 5 shows that the water-methane interfacial surface tension decreases with temperature and varies little with pressure. These trends as well as the range of interfacial surface tension are consistent with earlier simulations.<sup>38</sup> Using the interfacial tension in Fig. 5, the prediction of the gas breakthrough pressure by the classical capillary theory is computed as  $P_c^0 = 2\gamma/W$  and shown in Fig. 4. We observe that the gas breakthrough pressure is systematically underestimated using this method. In this method, however, the residual water film, which effectively narrows the pore, is neglected. To consider this effect, we compute a corrected capillary pressure  $P_c^1 = \gamma/(W/2 - h)$  (h is the thickness of the residual film), and the predicted gas breakthrough pressure is shown with solid line in Figure 5. The corrected capillary pressure can predict the gas breakthrough pressure in the 4nm- and 6nm-wide pores reasonably well, but still underestimates the gas breakthrough pressure in the 2nm-wide pores by ~20MPa. The significant underestimation of the gas breakthrough pressure by the corrected capillary pressure is next examined from several perspectives.

It is possible that the pore entrance can contribute an extra energy barrier for gas invasion into the nanopores. Since this possible entrance effect is not taken into account in the classical capillary theory, it can cause the underestimation of gas breakthrough pressure by the capillary theory. However, this effect is ruled out through additional simulations. In these simulations, we start from a configuration in which the gas has already invaded into the 2nm-wide nanopores by half the pore length under high pressure (e.g., the pressure marked by the two red squares in Fig. 5). We then lower the pressure difference  $\Delta P_{ud}$  between the two pistons to the highest pressure difference at which gas breakthrough was not observed in the simulations described in Section 2 (e.g., the pressure marked by the rightmost blue star in Fig. 5). It is found that, within 30-40ns, the gas front always recedes back into the upstream reservoir. This thus rules out the existence of an extra barrier when the gas break into a pore initially filled by liquids.

It is possible that the interfacial tension of the water-gas interfaces inside the nanopore differs from that at planar water-gas interfaces because of their small radius. However, prior work showed that interfacial tension decreases as the radius of the interfaces approaches molecular dimension,<sup>39</sup> which should lead to the overestimation of the breakthrough pressure when the interfacial tension measured for planar water-gas interfaces is used.

In addition to the capillary pressure, the disjoining pressure of the water film inside the pore may pose an additional barrier for gas invasion. Indeed, recent simulations revealed that disjoining pressure is responsible for the anomalous infiltration pressure observed in some carbon nanotubes.

40 Since the mica surface is not charged, two types of disjoining pressure, i.e., the van der Waals disjoining pressure and the structural disjoining pressure, can be considered. The van der Waals disjoining pressure is given by

$$\Pi_{vdw} = -\frac{A}{6\pi W^3} \tag{2}$$

where A is the Hamaker constant. Taking A as  $2.0 \times 10^{-20}$ J from theoretical prediction<sup>41</sup> or  $2.2 \times 10^{-20}$ J from experimental measurement<sup>41</sup>, the magnitude of the van der Waals disjoining pressure

in a 2nm-wide pore is  $\sim$ 0.13MPa, too small to explain the observed discrepancy observed above. The structural disjoining pressure for a hard sphere liquid confined between two planar walls is given by  $^{40-41}$ 

$$\Pi_{stru} = -\rho_{\infty} k_B T \cos\left(\frac{2\pi W}{\sigma}\right) e^{-\frac{W}{\sigma}} \tag{3}$$

where  $\rho_{\infty}$  is the bulk density of the liquids,  $k_B$  is the Boltzmann constant, and  $\sigma$  is the diameter of fluid molecules. Taking the diameter of water molecule as 0.3nm, the magnitude of the structural disjoining pressure in 2nm-wide pores is thus ~0.11MPa, again too small to explain the observed discrepancy observed above.

The structural disjoining pressure in Equation (3), however, does not take into account the fact that the mica surface is hydrated by interfacial water molecules that bond strongly to them. When two mica surfaces approach each other closely, the hydration structure near individual mica surfaces can be perturbed, and the resulting hydration force can generate an additional structural disjoining pressure.<sup>41</sup>

To evaluate whether surface hydration can lead to the underestimation of the gas breakthrough pressure, we examine the hydration of the mica surfaces in both 2nm-wide and 4nm-wide pores. Figure 6a compares the water density profile as a function of distance from the mica wall in both pores. We observe that the water density profile shows oscillation only close to the mica surface and becomes uniform beyond  $\sim$ 0.5nm from the mica surface. Importantly, the density profile of intefacial water is pratically identical in both pores. Because water is a dipolar molecule and its intefacial structure is also characterized by its orientation, we further assess the orientation of the interfacial water in the 2nm- and 4nm-wide pores. As shown in Fig. 6b, we consider water molecules in two regions (region 1: W/2–0.3nm<z<W/2, W is the pore width; region 2: -0.2nm <z<0.5nm) and compute the distribution of the water molecules' dipole with respect to the normal direction of the mica surface. Figure 6c shows that the water molecules in Region 1 are nearly

randomly oriented. Water molecules in Region 2 tend to orient their dipole toward the mica surface. Importantly, in each region, the orientation of water molecules is nearly identical in the 2nm- and 4nm-wide pores. The fact that the density profile and the dipole orientation distribution of interfacial water in both pores are nearly identical suggests that the purtubration of the water structure near mica surface as the pore width decreases from 4 to 2nm is very small. Thereore, the hydration force and related disjoining pressure is unlikely to be significant. This is also consistent with previous experimental studies which showed that the hydration force between mica surface separated by water decays to nearly zero at a separation about 2nm. <sup>42</sup> Therefore, the hydration forces cannot cause the overestimation of the gas breakhrough pressure observed in Fig. 5.

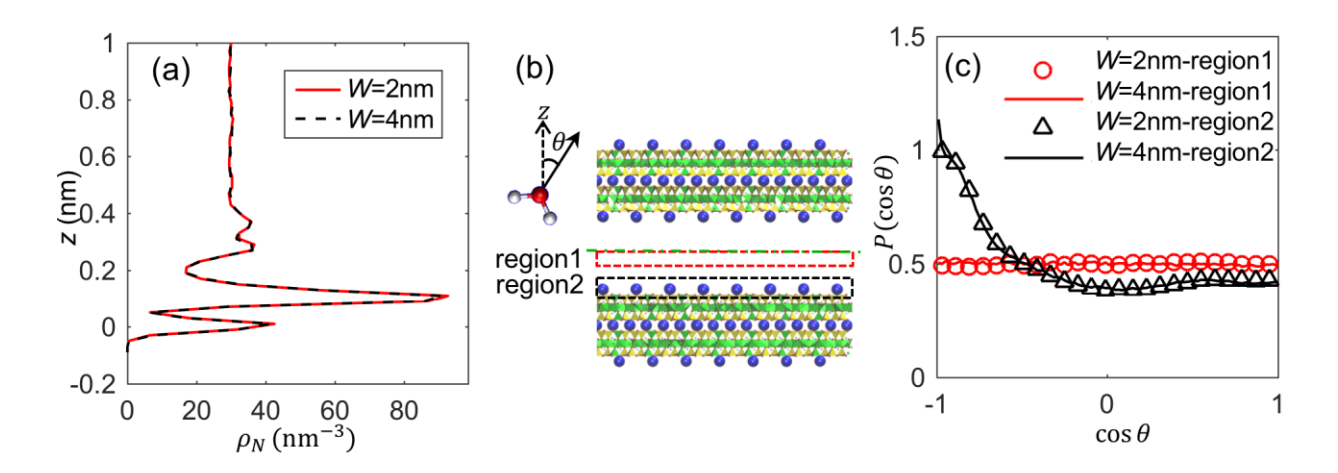


**Figure 6.** Density distribution and orientation of water molecules near mica-water interfaces in 2nm and 4nm-wide pores filled with water. (a) The water number density profiles along z-direction in the two pores. (b) A schematic showing the definition of region 1 (the red dashed box located at W/2-0.3nm< z < W/2, W is the pore width) and region 2 (the black dashed box located at -0.2nm< z < 0.5nm) in the mica pores. The dipole orientation of water molecules with respect to the normal direction of the nearest mica wall is calculated in these two regions. (c) The dipole orientation distribution of water in regions 1 and 2 (see panel b) for the 2 and 4nm-wide pores. A random distribution corresponds to  $P(\cos\theta) = 0.5$ .

None of the above physics can explain the underestimation of the gas breakthrough pressure using the classical capillary pressure, even after the pore width is corrected by considering the finite thickness (diffuseness) of the residual liquid film. Here we suggest that the discrepancy can originate from the ambiguity in precisely defining the width of a pore when it approaches

molecular dimensions. Specifically, due to thermal fluctuation, the liquid surface is diffuse and exhibits a finite thickness. Under the action of capillary forces, the thickness of a liquid-gas interface is  $\sim \sqrt{k_B T/\gamma}$ . With such a diffuseness of the liquid-gas interface, a thickness of  $h - 0.5\sqrt{k_B T/\gamma}$  to  $h + 0.5\sqrt{k_B T/\gamma}$  may be designated to a liquid film with a thickness of h computed using Equation (1). For a pore with a width of W and a residual liquid film with a thickness of h, the lower and upper limits of the effective pore width can be estimated reasonably by

$$W_{eff} = W - 2(h \pm \frac{1}{2}\sqrt{k_B T/\gamma}) \tag{4}$$

Using the new effective pore width to compute the capillary pressure, the range of reasonable breakthrough pressure for a given pore can be computed. The shaded area in Fig. 4 shows the range of possible gas breakthrough pressure when the range of film thickness to assign is estimated using Equation (4). For all pores considered here, the gas breakthrough pressure observed in the MD simulations is within the shaded area shown in Fig. 4. Therefore, the diffuseness of the gas-water interface can potentially explain why the gas breakthrough pressure is underestimated significantly in the 2nm-wide pores.

#### 3.3 Dynamics of gas invasion into liquid-filled pores

After gas breaks into a pore, the subsequent two-phase flow proceeds as a liquid meniscus moving deeper into the pore. Here we quantify the movement of the liquid meniscus by computing the position of its front (i.e., point O in Fig. 7a) and examine to what extent it can be described by the classical hydrodynamics. The forced invasion of gas into a liquid-filled pore can be predicted using the approach for deriving the Lucas-Washburn equation as in the case of the spontaneous imbibition of fluids into pores. Specifically, we make three assumptions: (1) inertia effects are negligible, (2) the gas breakthrough pressure can be computed using  $P_B = P_C^1 = \gamma/(W - 2h)$ , (3) the dynamics of gas invasion into a pore is dominated by the transport of liquids in the liquid-filled portion of the pore, and the latter can be treated as a simple Poiseuille flow with a slip length of b

on the pore walls. In the third assumption, the complex two-phase flow near the gas invasion front is neglected, which is reasonable only if the total thickness of the residual liquid films on the pore wall is much smaller than the pore width. With these assumptions, one can show that, in a pore that is initially filled entirely by liquids, the movement of the front of the liquid meniscus observes

$$(L - x)^2 = L^2 - 2At (5)$$

where L is the length of the pore, x is the position of the liquid meniscus front inside the pore, gas begins to invade into the pore at t=0 and A is a constant given by

$$A = \frac{W^2(W+6b)}{12\eta(W-2h)} (\Delta P_{ud} - P_B) \tag{6}$$

where  $\Delta P_{ud}$  is the pressure drop between the two liquid reservoirs.

The predictions of Equations (5-6) can be checked using MD simulation data. Because the total residual water film thickness on pore walls is ~35% of the width of the 2nm-wide pore, the third assumption underlying these equations is invalid in these pores. Therefore, we only examine the validity of Equations (5-6) in the 4nm- and 6nm-wide pores. The position of the liquid meniscus front is determined as follows. We compute the water density along the pore center at each time  $\rho_{cl}(x)$ , and scan from the pore entrance to the pore exit. The position at which the water density  $\rho_{cl}(x)$  reaches bulk water density (31.3nm<sup>-3</sup>) is considered as the front of the liquid meniscus. Figure 7a shows the dynamics of the meniscus front for a pressure difference  $\Delta P = 20$ MPa in the 4nm- and 6nm-wide pores. We observe that, except at the final stage of gas invasion process, the square of the length of the liquid-filled pore,  $(L-x)^2$ , decreases linearly with time, in agreement with the prediction by Equations (5-6). Linear regression of the data in Fig. 7a shows that the constant A in Equation 5 is  $77.6 \times 10^{-9}$  and  $53.2 \times 10^{-9}$ m<sup>2</sup>/s in the 4nm- and 6nm-wide pores, respectively. The deviation from the linear scaling of  $(L-x)^2$  with respect to time t during the final stage of gas invasion is caused by the fact that, at this stage, the liquid-filled portion of the pore is short and thus the hydrodynamic resistance for flow from the pore exit to the reservoir can

no longer be neglected (a similar effect is observed during the initial stage of liquid being imbibed into gas-filled pores). 44-45

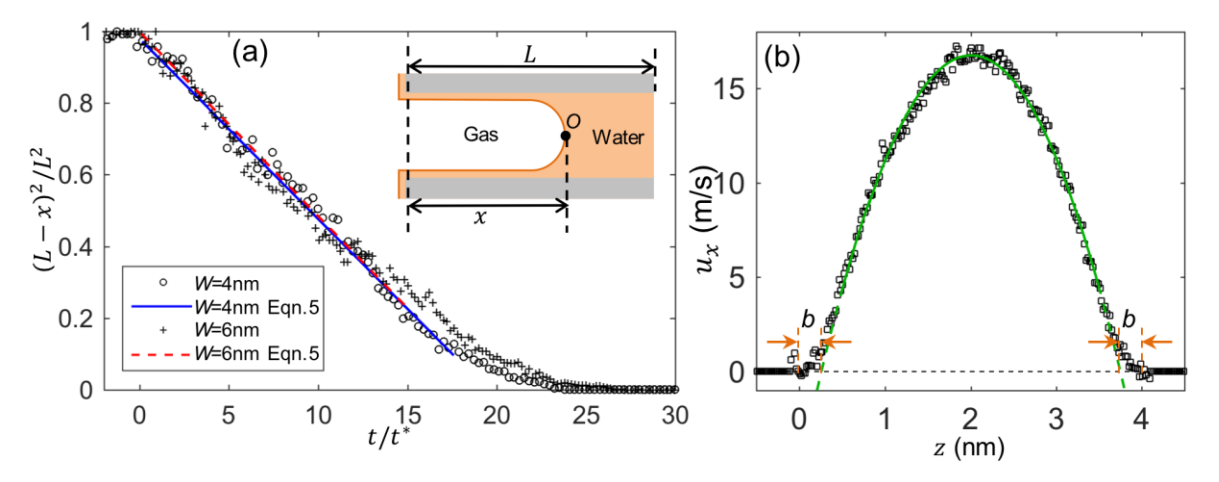


Figure 7. Dynamics of gas invasion into mica pores. (a) The location the liquid meniscus in the pore (x) as a function of time (t=0) is defined as the instant that gas starts to invade into the pore) for W=4 and 6nm pores. The meniscus position x is shown as  $(L-x)^2$  and normalized by  $L^2$ , where L is the pore length. The time is normalized by  $t^* = L/\sqrt{\Delta P_{ud}/\rho}$ , where  $\Delta P_{ud}$  is the pressure difference between the two liquid reservoirs up- and down-stream the pore and  $\rho$  is the bulk water density at 400K. The data points are linear fitted base on Equation 5. The inset shows a schematic of gas invading into a nanopore. (b) The x-velocity of water flow across a 4nm-wide pore driven by a constant acceleration. The velocity profile in the central portion of the pore is fitted to a quadratic curve and extrapolated to the wall to obtain the slip length b.

To check if the pre-factor A can be computed accurately by Equation (6), we determine the two parameters in this equation (viscosity  $\eta$  and slip length b) through separate simulations. Specifically, we build a 4nm-wide pore that is periodic in its length direction (i.e., no reservoirs at its two ends) and has identical mica walls with those in the gas invasion simulations. The pore is filled with water to the density found in the liquid-filled portion of 4nm-wide pores. To measure  $\eta$  and b, a constant acceleration is applied on each water molecule to generate a steady flow. The velocity profile of the resulting flow across the pore is shown in Fig. 7b and a parabolic velocity profile, as expected from classical hydrodynamics, is observed in the central portion of the pore. Fitting the velocity profile in the central portion of the pore, the viscosity  $\eta$  is calculated as 0.22mPa·s, which is close to the reported value of bulk water at the same temperature. <sup>46</sup> Extrapolating the parabolic velocity profile to the pore wall (see Fig. 7b), a negative slip length of

b=0.256nm is obtained. Such a negative slip length is consistent with the fact that water molecules are attracted strongly to the pore walls.<sup>47</sup> Using the  $\eta$  and b computed here, as well as the residual film thickness determined in *Section 3.1*, the pre-factor A given by Equation 6 is computed to be  $73.4 \times 10^{-9}$  and  $56.5 \times 10^{-9}$ m<sup>2</sup>/s for 4nm- and 6nm-wide pores, respectively. Their good agreement with these extracted directly from Fig. 7b suggests that the classical hydrodynamic theories can be used to predict the invasion of gas into nanopores accurately down to a pore width of 4nm.

### 4. Conclusions

In summary, we study the invasion of methane gas into mica nanopores initially filled with water using MD simulations. Driven by sufficiently high pressure, the methane gas can invade into the mica pore and move downstream. However, a residual film is left behind the moving liquid meniscus. The thickness of this film is less than one nanometer in the pores studied here (2nm-, 4nm- and 6nm-wide) and decreases as the pore width decreases. The critical pressure for gas invasion, i.e., the gas breakthrough pressure, for the 4nm- and 6nm-wide pores can be predicted using the capillary pressure, providing that the curvature of the liquid meniscus is corrected using the finite thickness of the residual film on the mica walls. For the 2nm-wide pores, the capillary pressure corrected by the film thickness still underestimates the gas breakthrough pressure. This underestimation is unlikely to be caused by van der Waals and structural disjoining pressure as well as the hydration interactions, but can be rationalized by taking into account the diffuseness of the gas-liquid interface. The dynamics of gas invasion, as quantified using the movement of the front of the liquid meniscus, can be predicted by the classical hydrodynamics if the negative slip length on the mica surface, which originates from the strong affinity of water to the hydrophilic mica surface, is taken into account. These results suggest that the gas invasion into liquid-filled nanopores can be described by continuum theories as pores are as narrow as 2nm providing that crucial interfacial effects such as the existence and finite thickness of the residual liquid film,

diffuseness of the gas-liquid interfaces, and the negative slip length at solid-liquid interfaces are taken into account.

Gas invasion in practical engineering systems, e.g., porous media saturated with water, is much more complicated than the ideal situation considered here. For example, there often exist heterogeneity in surface properties (e.g., hydrophobic vs. hydrophilic), pore size, and pore shape along the path of gas invasion. However, delineating the essential features of the gas invasion in the model systems adopted here and clarifying the validity of continuum theories in describing the thermodynamics (e.g., the gas breakthrough pressure) and dynamics (e.g., the movement of liquid meniscus) of the gas invasion process is a key step toward obtaining a fundamental understanding of the gas invasion in more practical situations.

## Acknowledgement

We thank the ARC at Virginia Tech for generous allocations of computer time. R.Q. gratefully acknowledges the support from NSF (CBET 1705287).

### References

- 1. Liu, L.; Chen, X.; Lu, W.; Han, A.; Qiao, Y., Infiltration of Electrolytes in Molecular-Sized Nanopores. *Phys. Rev. Lett.* **2009**, *102*, 184501.
- 2. Tas, N. R.; Haneveld, J.; Jansen, H. V.; Elwenspoek, M.; van den Berg, A., Capillary Filling Speed of Water in Nanochannels. *Appl. Phys. Lett.* **2004**, *85*, 3274-3276.
- 3. Gruener, S.; Hofmann, T.; Wallacher, D.; Kityk, A. V.; Huber, P., Capillary Rise of Water in Hydrophilic Nanopores. *Phys. Rev. E* **2009**, *79*, 067301.
- 4. Schoch, R. B.; Han, J.; Renaud, P., Transport Phenomena in Nanofluidics. *Rev. Mod. Phys.* **2008**, 80, 839-883.
- 5. Duan, C.; Wang, W.; Xie, Q., Review Article: Fabrication of Nanofluidic Devices. *Biomicrofluidics* **2013**, *7*, 026501.
- 6. Dimitrov, D. I.; Milchev, A.; Binder, K., Capillary Rise in Nanopores: Molecular Dynamics Evidence for the Lucas-Washburn Equation. *Phys. Rev. Lett.* **2007**, *99*, 054501.
- 7. Das, S.; Mitra, S. K., Different Regimes in Vertical Capillary Filling. *Phys. Rev. E* **2013**, *87*, 063005.
- 8. Cao, G.; Qiao, Y.; Zhou, Q.; Chen, X., Infiltration Behaviour of Water in a Carbon Nanotube under External Pressure. *Philos. Mag. Lett.* **2008**, *88*, 371-378.

- 9. Supple, S.; Quirke, N., Rapid Imbibition of Fluids in Carbon Nanotubes. *Phys. Rev. Lett.* **2003**, *90*, 214501.
- 10. Yamashita, K.; Daiguji, H., Molecular Dynamics Simulations of Water Uptake into a Silica Nanopore. *J. Phys. Chem. C* **2015**, *119*, 3012-3023.
- 11. Mo, J.; Li, L.; Zhou, J.; Xu, D.; Huang, B.; Li, Z., Fluid Infiltration Pressure for Hydrophobic Nanochannels. *Phys. Rev. E* **2015**, *91*, 033022.
- 12. Oyarzua, E.; Walther, J. H.; Mejia, A.; Zambrano, H. A., Early Regimes of Water Capillary Flow in Slit Silica Nanochannels. *Phys. Chem. Chem. Phys.* **2015**, *17*, 14731-14739.
- 13. Helmy, R.; Kazakevich, Y.; Ni, C.; Fadeev, A. Y., Wetting in Hydrophobic Nanochannels: A Challenge of Classical Capillarity. *J. Am. Chem. Soc.* **2005**, *127*, 12446-12447.
- 14. Qiao, Y.; Punyamurtula, V. K.; Han, A.; Kong, X.; Surani, F. B., Temperature Dependence of Working Pressure of a Nanoporous Liquid Spring. *Appl. Phys. Lett.* **2006**, *89*, 251905.
- 15. Zhao, J.; Liu, L.; Culligan, P. J.; Chen, X., Thermal Effect on the Dynamic Infiltration of Water into Single-Walled Carbon Nanotubes. *Phys. Rev. E* **2009**, *80*, 061206.
- 16. Li, S.; Dong, M.; Li, Z.; Huang, S.; Qing, H.; Nickel, E., Gas Breakthrough Pressure for Hydrocarbon Reservoir Seal Rocks: Implications for the Security of Long-Term Co2 Storage in the Weyburn Field. *Geofluids* **2005**, *5*, 326-334.
- 17. Amann-Hildenbrand, A.; Ghanizadeh, A.; Krooss, B. M., Transport Properties of Unconventional Gas Systems. *Mar. Pet. Geol.* **2012**, *31*, 90-99.
- 18. Vincent, O.; Sessoms, D. A.; Huber, E. J.; Guioth, J.; Stroock, A. D., Drying by Cavitation and Poroelastic Relaxations in Porous Media with Macroscopic Pores Connected by Nanoscale Throats. *Phys. Rev. Lett.* **2014**, *113*, 134501.
- 19. Vincent, O.; Szenicer, A.; Stroock, A. D., Capillarity-Driven Flows at the Continuum Limit. *Soft matter* **2016**, *12*, 6656-6661.
- 20. Bui, K.; Akkutlu, I. Y., Nanopore Wall Effect on Surface Tension of Methane. *Mol. Phys.* **2015**, *113*, 3506-3513.
- 21. Vo, T. Q.; Barisik, M.; Kim, B., Near-Surface Viscosity Effects on Capillary Rise of Water in Nanotubes. *Phys. Rev. E* **2015**, *92*.
- 22. Ho, T. A.; Striolo, A., Water and Methane in Shale Rocks: Flow Pattern Effects on Fluid Transport and Pore Structure. *AIChE J.* **2015**, *61*, 2993-2999.
- 23. Malani, A.; Ayappa, K. G., Adsorption Isotherms of Water on Mica: Redistribution and Film Growth. *J. Phys. Chem. B* **2009**, *113*, 1058-1067.
- 24. Wang, J.; Kalinichev, A. G.; Kirkpatrick, R. J.; Cygan, R. T., Structure, Energetics, and Dynamics of Water Adsorbed on the Muscovite (001) Surface: A Molecular Dynamics Simulation. *J. Phys. Chem. B* **2005**, *109*, 15893-15905.
- 25. Ou, X.; Wang, X.; Lin, Z.; Li, J., Heterogeneous Condensation of Water on the Mica (001) Surface: A Molecular Dynamics Simulation Work. *J. Phys. Chem. C* **2017**, *121*, 6813-6819.
- 26. Martin, M. G.; Siepmann, J. I., Transferable Potentials for Phase Equilibria. 1. United-Atom Description of N-Alkanes. *J. Phys. Chem. B* **1998**, *102*, 2569-2577.

- 27. Cygan, R. T.; Liang, J.-J.; Kalinichev, A. G., Molecular Models of Hydroxide, Oxyhydroxide, and Clay Phases and the Development of a General Force Field. *J. Phys. Chem. B* **2004**, *108*, 1255-1266.
- 28. Argyris, D.; Cole, D. R.; Striolo, A., Ion-Specific Effects under Confinement: The Role of Interfacial Water. *ACS Nano* **2010**, *4*, 2035-2042.
- 29. Hess, B.; Kutzner, C.; Van Der Spoel, D.; Lindahl, E., Gromacs 4: Algorithms for Highly Efficient, Load-Balanced, and Scalable Molecular Simulation. *J. Chem. Theory Comput.* **2008**, *4*, 435-447.
- 30. Rexer, T. F.; Benham, M. J.; Aplin, A. C.; Thomas, K. M., Methane Adsorption on Shale under Simulated Geological Temperature and Pressure Conditions. *Energy Fuels* **2013**, *27*, 3099-3109.
- 31. Bussi, G.; Donadio, D.; Parrinello, M., Canonical Sampling through Velocity Rescaling. *J. Chem. Phys.* **2007**, *126*, 014101.
- 32. Darden, T.; York, D.; Pedersen, L., Particle Mesh Ewald: An N·Log(N) Method for Ewald Sums in Large Systems. *J. Chem. Phys.* **1993**, *98*, 10089-10092.
- 33. Malani, A.; Ayappa, K., Adsorption Isotherms of Water on Mica: Redistribution and Film Growth. *J. Phys. Chem. B* **2009**, *113*, 1058-1067.
- 34. Khaneft, M.; Stühn, B.; Engstler, J.; Tempel, H.; Schneider, J. J.; Pirzer, T.; Hugel, T., Imbibition of Polystyrene Melts in Aligned Carbon Nanotube Arrays. *J. Appl. Phys.* **2013**, *113*, 074305.
- 35. Fang, C.; Qiao, R., Surface Hydration Drives Rapid Water Imbibition into Strongly Hydrophilic Nanopores. *Phys. Chem. Chem. Phys.* **2017**, *19*, 20506-20512.
- 36. Davis, H. T., Statistical Mechanics of Phases, Interfaces, and Thin Films; Wiley-VCH, 1996.
- 37. Yuet, P. K.; Blankschtein, D., Molecular Dynamics Simulation Study of Water Surfaces: Comparison of Flexible Water Models. *J. Phys. Chem. B* **2010**, *114*, 13786-13795.
- 38. Kashefi, K.; Pereira, L. M.; Chapoy, A.; Burgass, R.; Tohidi, B., Measurement and Modelling of Interfacial Tension in Methane/Water and Methane/Brine Systems at Reservoir Conditions. *FFE* **2016**, *409*, 301-311.
- 39. Tolman, R. C., The Effect of Droplet Size on Surface Tension. J. Chem. Phys. 1949, 17, 333-337.
- 40. Gravelle, S.; Ybert, C.; Bocquet, L.; Joly, L., Anomalous Capillary Filling and Wettability Reversal in Nanochannels. *Phys. Rev. E* **2016**, *93*, 033123.
- 41. Israelachvili, J. N., *Intermolecular and Surface Forces*; Academic press, 2015.
- 42. Leng, Y., Hydration Force between Mica Surfaces in Aqueous Kcl Electrolyte Solution. *Langmuir* **2012**, *28*, 5339-5349.
- 43. Aarts, D. G.; Schmidt, M.; Lekkerkerker, H. N., Direct Visual Observation of Thermal Capillary Waves. *Science* **2004**, *304*, 847-850.
- 44. Oyarzua, E.; Walther, J. H.; Mejía, A.; Zambrano, H. A., Early Regimes of Water Capillary Flow in Slit Silica Nanochannels. *Phys. Chem. Chem. Phys.* **2015**, *17*, 14731-14739.
- 45. Joly, L., Capillary Filling with Giant Liquid/Solid Slip: Dynamics of Water Uptake by Carbon Nanotubes. *J. Chem. Phys.* **2011**, *135*, 214705.
- 46. Lee, S. H., Molecular Dynamics Simulation Study for Shear Viscosity of Water at High Temperatures Using Spc/E Water Model. *Bull. Korean Chem. Soc.* **2014**, *35*, 644-646.
- 47. Thompson, P. A.; Robbins, M. O., Shear Flow near Solids: Epitaxial Order and Flow Boundary

Conditions. Phys. Rev. A 1990, 41, 6830.